Heliyon 10 (2024) e38057

Contents lists available at ScienceDirect

Heliyon

journal homepage: www.cell.com/heliyon

Research article

Facile construction of Mo-based nanozyme system via ZIF-8 templating with enhanced catalytic efficiency and antibacterial performance

Haoruo Jia [a,b,c,1], Ziyuan Zheng [d,1], Jining Qu [a,b,c,1], Hongtao Yu [e], Zhoujun Zhu [f], Qingda Lu [a,b,c], Fei Su [a,b,c], Yating Yang [a,b,c], Tongtong Feng [g], Qiang Jie [a,b,c,*]

[a] *Pediatric Orthopaedic Hospital, Honghui Hospital, Xi'an Jiaotong University, Xi'an, 710054, China*
[b] *Clinincal Research Center for Pediactric Skeletal Deformity and Injury of Shaanxi Province, Xi'an, 710054, China*
[c] *Xi'an Key Laboratory of Skeletal Developmental Deformity and Injury Repain, Xi'an, 710054, China*
[d] *School of Environmental Science and Engineering, Changzhou University, Changzhou, 213164, China*
[e] *First Affiliated Hospital, Shihezi University, Shihezi, 832008, China*
[f] *Department of Joint Surgery, Sixth Affiliated Hospital, Xinjiang Medical University, Urumqi, 830092, China*
[g] *Xi'an Medical University, Xian, 710068, China*

ARTICLE INFO

Keywords:
Single-atom nanozymes
Molybdenum
Enzymatic cascade
Antibacterial activity

ABSTRACT

Although Zeolitic Imidazolate Framework-8 (ZIF-8) shows significant promise in chemodynamic therapy of bacterial infections due to its large specific surface area and enzyme-like activity, it still faces a considerable gap compared to natural enzymes. The dependency on low pH and high concentrations of hydrogen peroxide ((H_2O_2)) is a major factor limiting the clinical progress of nanozymes. Single-atom nanozymes (SA-zyme), which exhibit superior catalytic performance, are expected to overcome this limitation. In this study, we used ZIF-8 as a template to prepare structurally regular molybdenum-based single-atom nanozymes (Mo-zyme) by coordinating molybdenum atoms with nitrogen atoms within the zeolitic imidazolate framework and evaporating the zinc element at high temperatures. The cascade catalytic performance of the nanodrugs was enhanced by loading glucose oxidase (GOx) and encapsulating it with a hyaluronic acid (HA) layer to form a composite (Mo/GOx@HA). Upon contact with hyaluronidase from bacteria in infected tissues, the cascade reaction is triggered, resulting in the degradation of the HA shell, and releasing the encapsulated GOx. Once exposed, GOx catalyzes the oxidation of glucose into gluconic acid, resulting in a localized decrease in pH and continuous production of H_2O_2. The combination of lowered pH and increased H_2O_2 concentration significantly amplifies the catalytic activity of the Mo-zyme. This enhanced activity facilitates the in situ generation of hydroxyl radicals (•OH) on the bacterial surface, leading to effective and efficient bacterial eradication. Wound infection treatment has demonstrated that the as-prepared Mo/GOx@HA exhibits excellent antibacterial and anti-inflammatory activity. This work provided a promising enzymatic cascade reaction nanoplatform for the treatment of bacteria infected wounds.

* Corresponding author. Pediatric Orthopaedic Hospital, Honghui Hospital, Xi'an Jiaotong University, Xi'an, 710054, China
E-mail addresses: jieqiangchina@med.nwu.edu.cn, jieqiangxjhh@126.com (Q. Jie).
[1] These authors contributed equally to this work.

https://doi.org/10.1016/j.heliyon.2024.e38057
Received 16 July 2024; Received in revised form 3 September 2024; Accepted 17 September 2024
Available online 18 September 2024

1. Introduction

Bacterial infections have long posed a serious threat to human health and survival. Skin injuries and surgical procedures increase the risk of exposing wounds [1–3]. While antibiotics effectively improve outcomes in such cases, the issue of antibiotic resistance, exacerbated by overuse, remains a persistent concern for patients and clinicians alike [4,5]. Recent advancements in nanomedicine have significantly improved the delivery of antibiotics through implantable biomaterials like bioceramics or hydrogel patches [6,7]. However, these innovations only delay rather than solve the problem of resistance. In contrast to conventional drug treatments, a promising new strategy has emerged in recent years: utilizing endogenous substances to catalyze the production of reactive oxygen species (ROS) [8–10]. ROS can inflict irreversible oxidative stress damage on bacterial DNA. This approach is appealing because it avoids resistance issues, and the effectiveness of ROS generation directly influences bacterial eradication [11–13]. Despite its potential, the complex extraction process and high cost associated with natural enzymes remain significant barriers to widespread adoption [14]. Therefore, finding simpler methods to develop antibacterial materials with enzyme-like activity remains a critical challenge.

Metal-derived nanoparticles have garnered significant attention in recent years for their adjustable surface area, pore size, and particle dimensions, making them pivotal in environmental protection, energy catalysis, and biomedical applications [15]. As a representative of nanozymes, it also exhibits unique enzyme-mimicking properties, enhancing its potential for use in catalytic and therapeutic applications, where its stability and efficiency can be finely tuned for specific needs [16]. However, its inherent structural heterogeneity creates a disparity in catalytic activity compared to natural enzymes, thereby limiting its effectiveness in antibacterial applications [17–19]. Single-atom nanoenzymes (SA-zymes) offer significant advantages over traditional nanozymes by maximizing atomic efficiency. Traditional nanozymes often suffer from limited active site exposure and lower catalytic efficiency, whereas SA-zymes ensure that nearly every atom contributes to the catalytic process. This leads to enhanced activity, stability, and specificity, effectively bridging the performance gap between natural and artificial enzymes [20–22]. Nevertheless, the advent of SA-zymes does not signify flawless development of nanoenzyme-based antibacterial agents [23,24]. Challenges such as inadequate nanoenzyme-substrate contact, unstable drug encapsulation by nanoenzymes, weak nanoenzyme-bacteria binding, and physiological factors like pH and H_2O_2 levels in the environment hinder the optimal utilization of SA-zymes' high catalytic efficiency [24–26]. Additionally, exogenous H_2O_2 supplementation, while potentially enhancing catalytic activity, risks inducing immunogenicity, inflammation, and damage to normal tissues [27–29]. Hence, developing an efficient catalytic system based on SA-zymes remains indispensable for effective bacterial treatment.

Given the remarkable peroxidase-like activity of molybdenum-based nanozymes in nanobiomedicine [30,31], we introduce a streamlined synthesis method for molybdenum single-atom nanozymes (Mo-zyme) using a "host-guest" strategy with ZIF-8 as a template. We further utilize this Mo-zyme as a carrier for glucose oxidase (GOx), with hyaluronic acid (HA) electrostatically coating

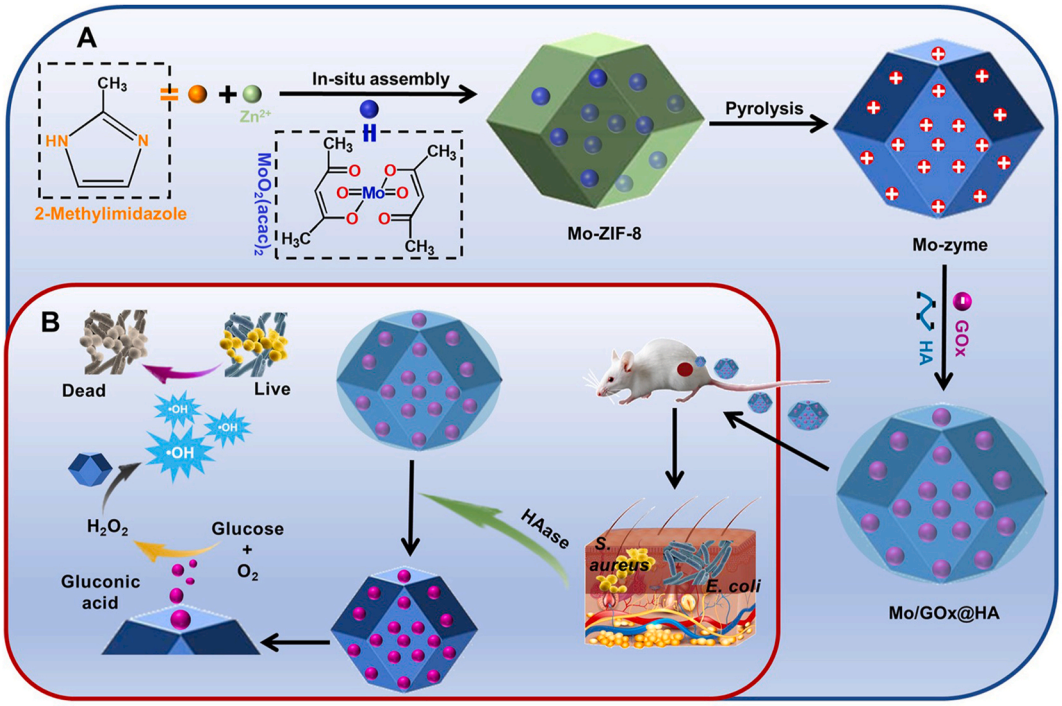

Scheme 1. (A) Schematic for the preparation of Mo/GOx@HA, (B) Illustration of the cascade catalytic reaction of Mo/GOx@HA as a self-activating nanoreactor for antibacterial.

the Mo-zyme surface to encapsulate GOx and prevent premature release (Scheme 1A). Upon encountering an infection, bacterial hyaluronidase (HAase) degrades the HA coating, releasing and exposing GOx, thus activating the antibacterial cascade. GOx then catalyzes the conversion of glucose into gluconic acid and hydrogen peroxide (H_2O_2) at the infection site. The resultant pH reduction from gluconic acid enhances Mo-zyme's catalytic activity, facilitating increased •OH production (Scheme 1B). This cascade-driven antibacterial process is crucial for its ability to enhance antibacterial efficacy while minimizing reliance on high concentrations of exogenous H_2O_2, thereby reducing potential side effects. It underscores the potential of this nanoplatform to overcome the limitations of traditional antibiotics, offering a promising alternative for developing effective antibacterial treatments.

2. Experimental section

2.1. Reagents and apparatus

2-methylimidazole, $Zn(NO_3)_2•6H_2O$, $MoO_2(acac)_2$, were purchased from Sinopharm Chemical Reagent Co., Ltd. (China), HA, 3,3,5,5-tetramethylbenzidine (TMB), glucose, and terephthalic acid (TA) were purchased from Aladdin Chemical Reagent Co., Ltd (China). GOx and hyaluronidase were purchased from Sigma-Aldrich (USA). Cell counting kit-8 (CCK-8), LIVE/DEAD BacLight Bacterial Viability Kit, and LB broth were purchased from Thermo Fisher Scientific Co., Ltd. (USA). DMEM medium, fetal bovine serum (FBS), and trypsin were purchased from Gibco Life Technologies (USA). Enhanced BCA Protein Assay Kit and 2.5 % glutaraldehyde were purchased from Beyotime Biotechnology (China). All other unspecified chemicals used in this study were of analytical or biochemical reagent grade and were employed following the received standards.

Scanning Electron Microscopy (SEM) images were acquired using a scanning electron microscope (Zeiss, Germany), while Transmission Electron Microscopy (TEM) images were obtained using a transmission electron microscope (JEOL, Japan). The zeta potential and hydrated particle size measurements were conducted using a dynamic light scattering (DLS) instrument, model FPMRC-PA-200I (Malvern, UK). X-ray diffraction (XRD) patterns were recorded from powdered samples with a D/max 2500 PC X-ray diffractometer (Rigaku, Japan). Fourier-transform infrared (FTIR) spectra for the various samples were obtained using an IRTracer-100 spectrometer (Shimadzu, Japan). Additionally, water contact angles were measured with a DSA25 standard contact angle goniometer (KRÜSS, Germany). A model U-3900 UV–vis spectrophotometer (Hitachi, Japan) was used for the determination of GOx concentration according to the standard curve predetermined.

2.2. Preparation of Mo-zyme and Mo/GOx@HA

Mo-zyme was synthesized using Zeolitic Imidazolate Framework-8 (ZIF-8) as a template through a "host-guest" strategy. In brief, 1666 mg of $Zn(NO_3)_2•6H_2O$ and 130 mg of $MoO_2(acac)$ were dispersed in 40 mL of methanol and subjected to ultrasonication for 30 min [32]. Following this, 80 mL of methanol solution containing 2-methylimidazole at a concentration of 46.25 mg/mL was added, and the mixture was magnetically stirred at room temperature for 12 h. The resulting Mo-ZIF-8 was obtained by centrifugation at 12, 000 rpm with methanol washing, followed by freeze-drying. The dried powder was then thermally treated at 900 °C under a nitrogen atmosphere for 3 h to obtain Mo-zyme in the form of black powder.

A HA coating was utilized to enhance the encapsulation efficiency of Mo-zyme with glucose oxidase (GOx). In a typical encapsulation process, Mo-zyme, GOx, and HA were mixed at a mass ratio of 1:2:1 at low temperature (~4 °C). The mixture was stirred under dark for 12 h and subsequently centrifuged. The resulting precipitate was freeze-dried to obtain Mo/GOx@HA. The GOx loading and encapsulation rate of Mo-zyme to GOx was determined by BCA method.

For the control experiment, Mo/GOx was prepared following the same method as above, with the exception of omitting HA during the encapsulation process.

2.3. Peroxidase-like catalytic activity evaluation of Mo-zyme

To investigate the peroxidase-like activity of Mo-zyme, TMB was used as the substrate in a reaction mixture containing 1 mM H_2O_2, 5 mM TMB, and 50 μg/mL Mo-zyme in 4 mL of 0.01 M PBS at pH 3.0. The catalytic reaction was monitored at 652 nm using a UV–vis spectrophotometer for 5 min at room temperature. Subsequently, the peroxidase-like catalytic activity of Mo-zyme at different pH values was assessed by adjusting the pH of the reaction system as described. The maximum catalytic activity of Mo-zyme was considered as 100 %, and the residual catalytic activity of Mo-zyme at other pH values was expressed as a percentage of the maximum activity.

For detection of hydroxyl radicals (•OH), TA was utilized as a fluorescent probe, which undergoes conversion to the highly fluorescent product 2-hydroxy terephthalic acid (TAOH) upon activation by •OH. H_2O_2 was dispersed in 4 mL of 0.01 M PBS at pH 3.0, with a reaction mixture containing 5 mM H_2O_2, 0.5 mM TA, and 50 μg/mL Mo-zyme. After incubation in darkness for 12 h, the fluorescence intensity of TAOH was measured using a fluorescence spectrophotometer.

2.4. Catalytic performance of Mo-zyme

The performance of GOx in catalyzing glucose conversion to gluconic acid under varying pH conditions was investigated. The catalytic reaction was conducted in 4 mL of 0.5 mM PBS at pH 7.0, with concentrations of 5 μg/mL GOx and 5 mM glucose. Control experiments using PBS with only glucose or GOx were also prepared. Subsequently, the cascade catalytic activity based on Mo-zyme

was evaluated at 37 °C for 90 min. A mixture containing 5 μg/mL GOx and 5 mM glucose was used to study the effect of glucose concentration on pH, with 0.001 % methyl red added to monitor color changes. The reaction systems included: (1) PBS, (2) glucose, (3) Mo/GOx, (4) glucose + Mo-SAzyme, (5) glucose + GOx, and (6) glucose + Mo/GOx.

To quantify the catalytic performance of Mo-zyme, additional reactions were conducted in 0.5 mM PBS at pH 7.4. Concentrations of Mo-zyme, GOx, glucose, and TMB were 100 μg/mL, 5 μg/mL, 5 mM, and 1 mM, respectively. The reactions proceeded at 37 °C for 3 h, after which color changes and absorbance at 652 nm were recorded for each system.

2.5. Responsive cascade catalytic performance of Mo/GOx@HA

100 μg/mL Mo/GOx@HA was exposed to 150 U/mL HAase at room temperature for 1 h. Subsequently, 5 mM glucose and TMB were added to the solution, which was shaken for 3 h at room temperature. The pH of the solution and absorbance at 652 nm were then measured. To assess the cascade catalytic effect, a similar process was conducted without HAase. Control experiments included Mo/GOx treated with glucose and TMB.

2.6. Antibacterial activity of Mo/GOx@HA in vitro

Single colonies of *S. aureus* or *E. coli* from LB-agar plates were transferred to LB broth and cultured with shaking at 37 °C for 8 h to reach the logarithmic growth phase. The bacterial suspensions were then diluted to a concentration of 1×10^7 CFU/mL. The bacterial suspensions were then subjected to different treatments: (1) PBS, (2) glucose, (3) Mo/GOx@HA, (4) glucose + Mo-zyme, (5) glucose + GOx, and (6) glucose + Mo/GOx@HA. Each treatment was incubated separately at 37 °C under agitation at 120 rpm for 8 h, with glucose and Mo/GOx@HA concentrations maintained at 15 mM and 100 μg/mL, respectively. After incubation, the bacterial suspensions were diluted 10,000-fold. Then, 100 μL of each diluted suspension was spread onto LB agar plates and cultured at 37 °C for 24 h. Colony counting on the agar plates was performed to evaluate the antibacterial effectiveness of each treatment.

2.7. Safety evaluation of Mo/GOx@HA

Hemocompatibility of Mo/GOx@HA: Whole mouse blood was collected into heparinized tubes to prevent coagulation, and fresh red blood cells (RBCs) were obtained and diluted to 2 % in saline. Mo-zyme or Mo/GOx@HA at a concentration of 1 mg/mL was added to the 2 % RBCs suspensions to achieve a final concentration of 500 μg/mL. Positive control samples were treated with deionized water, while negative control samples were treated with saline. All samples were statically incubated at 37 °C for 12 h. Supernatants were collected, and absorbance at 560 nm was measured. Hemolysis ratio was calculated using the formula [33]:

$$\text{Hemolysis ratio (\%)} = (\text{sample absorbance} - \text{negative control absorbance}) (\text{positive control absorbance} - \text{negative control absorbance}) \times 100. \quad (1)$$

Cytotoxicity assessment of Mo/GOx@HA: The cytotoxicity of was performed using a CCK-8 assay on HUVEC and NRK cells. Cells were seeded in 96-well plates (5×10^3 cells per well) and cultured for 24 h at 37 °C with 5 % CO_2. The medium was then replaced with medium containing Mo/GOx@HA at various concentrations, followed by incubation for another 24 h. Cell viability was determined using a microplate reader at 450 nm.

Additionally, Mo/GOx@HA was injected into BALB/c mice via the caudal vein at a dosage of 5 mg/kg, and main organs and serum were collected after 3 days. Blood biochemical analyses and HE staining were conducted to evaluate the biological safety of the Mo/GOx@HA nanoreactor in vivo.

2.8. Treatment of wound infection in vivo

A wound infection model was developed in male BALB/c mice (6–8 weeks old) as follows: Initially, a circular wound with a diameter of 6 mm was created on the mouse skin, followed by injection of *S. aureus* (3×10^7 CFU, 50 μL) into the wound. After 24 h, the *S. aureus*-infected mice were randomly divided into six groups (n = 5) and treated with: (1) PBS, (2) glucose, (3) Mo/GOx@HA, (4) glucose + Mo-zyme, (5) glucose + GOx, (6) glucose + Mo/GOx@HA. Treatments were applied to the wounds of each group every 24 h. Glucose and Mo/GOx@HA were administered at volumes of 50 μL, with concentrations of 15 mM and 100 μg/mL, respectively.

The infected wounds of mice in each group were monitored and photographed every other day. After 7 days, the infected wound tissues were homogenized in 1 mL of sterile saline and incubated at 37 °C for 24 h. Bacterial analysis was performed using the plate colony method, and the sections of the wound tissue from mice were subjected to H&E staining, Masson staining, and interleukin-6 immunofluorescence staining for histological and immunological evaluation.

2.9. Statistical analysis

Statistical analyses were performed using SPSS 20.0 (SPSS, Chicago) or R software (https://www.r-project.org). Data are presented as mean ± SD from at least triplicate measurements. Data analysis included Student's t-test (two-tailed), Pearson correlation coefficient test, Wilcoxon test, and repeated-measures analysis of variance (ANOVA). Statistical significance was set at $P < 0.05$.

3. Results and discussion

3.1. Synthesis and characterization of Mo-zyme system

As described in Scheme 1A, the preparation method of Mo-zyme begins by integrating molybdenum acetylacetonate into the ZIF-8 framework to form a molybdenum-containing precursor (Mo-ZIF-8). High-temperature pyrolysis then volatilizes the zinc ions, leaving molybdenum atoms embedded in a nitrogen-rich, porous carbon framework, resulting in Mo-zyme with enhanced catalytic properties. The elemental content variations presented in Table S1 provide preliminary support for this reaction process. SEM and TEM are employed to characterize the morphological features of the materials, examining the impact of Mo doping and high-temperature pyrolysis on nanoparticle structure. Compared to the well-defined dodecahedral structure of ZIF-8 in Fig. S1, the Mo-ZIF-8 synthesized using the template method does not exhibit significant morphological changes (Fig. 1A and B). Additionally, the crystallographic data in Fig. S2 reveal that the XRD pattern of Mo-ZIF-8 remains highly consistent with that of standard ZIF-8. This indicates that the Mo doping process, which involves introducing $MoO_2(acac)_2$ as an additive into ZIF-8, successfully preserves the nanoparticle structure without causing any damage.

After undergoing high-temperature pyrolysis, the Mo-zyme retains its dodecahedral structure, despite a slight reduction in size (~20 nm) (Fig. 1C and D). However, subtle changes in surface potential are detected by dynamic light scattering (DLS), as shown in Fig. S3. The Zeta potential of Mo-zyme increases by approximately 11.50 mV after pyrolysis, likely due to structural contraction and atomic exposure. Notably, no significant metal phases are observed in the high-angle annular dark-field scanning transmission electron microscopy (HAADF-STEM) images (Fig. 1E), where the red arrows mark the high-density bright spots corresponding to Mo single atoms. Energy-dispersive EDS further confirms the uniform distribution of C, N, and Mo throughout the nanostructure, suggesting that Mo atoms are successfully embedded into the nitrogen-doped carbon matrix [34,35].

XPS and XRD are used to further analyze the coordination environment and crystalline characteristics of the Mo single atoms. As shown in Fig. S4A, the N K-edge spectrum displays three distinct peaks at approximately 398, 400, and 403 eV, corresponding to the p*-transitions of pyridinic N, pyrrolic N, and graphitic N species, respectively [36]. Previous studies demonstrate that pyridinic N or pyrrolic N species can provide p-electrons to the π-conjugated structure [37]. Consistent with this, the Mo 3d-edge exhibits an electronic structure capable of forming π-conjugation (Fig. S4B), indicating that the nitrogen-doped carbon substrate after pyrolysis is capable of coordinating with Mo to form a single-atom dispersed complex. The uniform distribution of Mo atoms within the nanostructure, as evidenced by the absence of distinct crystalline features in the XRD pattern of Mo-zyme in Fig. S5, further suggests its amorphous nature.

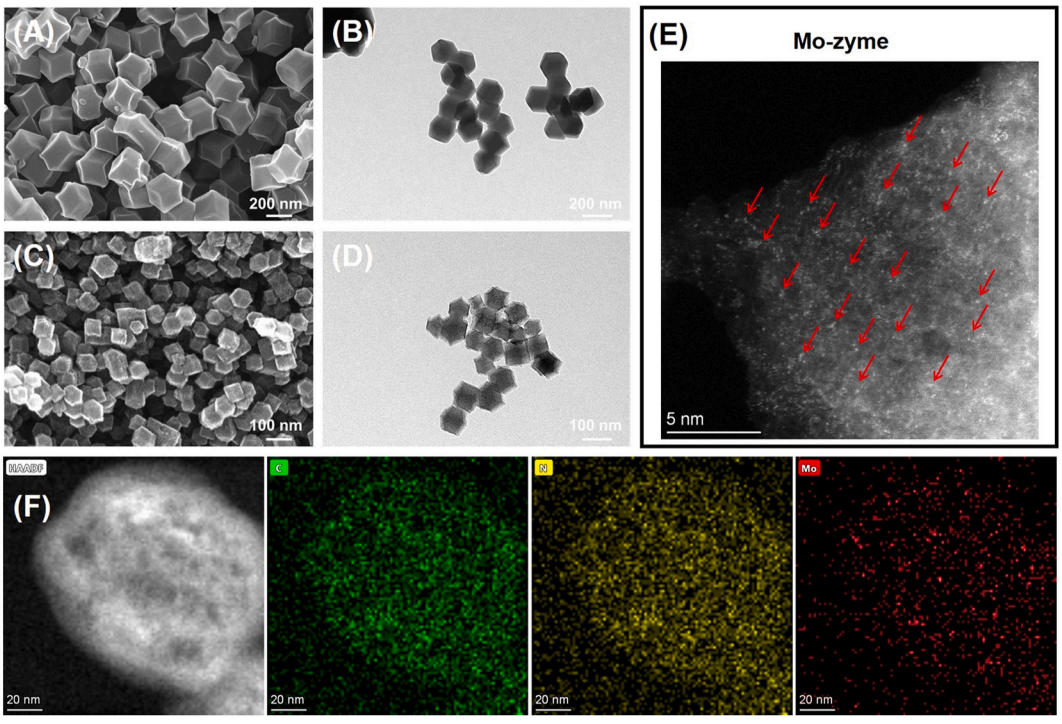

Fig. 1. (A) SEM images of Mo-ZIF 8, (B) TEM images of Mo-ZIF 8, (C) SEM images of Mo-zyme, (D) TEM images of Mo-zyme, (E) HAADF-STEM image of Mo-zyme, highlighting the atomically dispersed Mo atoms as bright dots, (F) EDS elemental mapping of Mo-zyme.

3.2. Study of GOx loading and HA encapsulation process

HA as a typical amorphous biopolymer, usually exhibits strong and broad diffraction peaks in XRD analysis (Fig. S5). However, when used to encapsulate Mo-zyme, the resulting Mo@HA retains its amorphous characteristics while primarily displaying the crystalline diffraction features of HA. This suggests that HA is a promising material for encapsulating Mo-zyme. To verify GOx loading in Mo-zyme using HA as an encapsulant, FTIR spectra of HA, GOx, Mo-zyme, and Mo/GOx@HA are analyzed (Fig. S6). Characteristic peaks at ~1650 cm^{-1} and ~1545 cm^{-1} attributed to amide I (–CO– and –CN– stretching) and amide II (–NH– bending) are evident in HA and GOx [38]. The total area proportion of amide I and amide II peaks are 9.85 % and 6.32 % in HA and GOx, respectively, but turned to 8.11 % in Mo/GOx@HA, confirming successful GOx encapsulation within Mo-zyme by HA.

Zeta potential measurements of Mo-zyme, GOx, HA, and Mo/GOx@HA using dynamic light scattering revealed significant changes (Fig. 2A). Mo-zyme exhibits a pronounced decrease in Zeta potential upon binding with GOx and HA due to electrostatic interactions, resulting in a weak negative charge (~3.00 ± 1.06 mV). Conversely, Mo/GOx initially shows an increase in Zeta potential on the first day followed by a decrease over the next six days, demonstrating the stability imparted by HA encapsulation (Fig. 2B). Hydration particle size tests (Fig. S7) indicate a slight increase in Mo/GOx@HA particle size, which is attributed to the presence of HA promoting hydration layer formation. However, particle size remains stable over seven days (Fig. 2C), highlighting HA's role in maintaining particle size stability, crucial for biomedical applications where nanoparticle stability in biological fluids is essential.

The UV–vis spectrum is utilized to assess the encapsulation efficiency of GOx in Mo-zyme using HA as the enzyme-sensitive coating. As depicted in Fig. 2D, a characteristic absorption peak of GOx at ~265 nm is evident, while Mo-zyme and HA do not exhibit significant peaks at this wavelength. Notably, a weak peak observed in Mo/GOx@HA indicates successful encapsulation of GOx within Mo-zyme. Additionally, HA is known for its high hydrophilicity, a critical property influencing biological performance in nanomedicine. Contact angle measurements (Fig. 2E) demonstrate significantly enhanced hydrophilicity in Mo/GOx@HA, attributed to HA coating that exposes polar groups on the Mo/GOx surface, confirming successful preparation [38]. The encapsulation ratio and loading ratio of GOx in Mo-zyme are calculated as 83.26 % and 13.19 %, respectively, based on the standard curve of GOx (Fig. S8). Regarding drug release kinetics, Fig. 2F illustrates rapid release of GOx from Mo/GOx, indicating physical adsorption with limited. Conversely, the release profile of GOx from Mo/GOx@HA in PBS at pH 7.4 suggests a slow-release behavior facilitated by HAase-mediated degradation of HA. This finding supports the potential for cascade catalysis in future antibacterial applications.

3.3. Catalytic activity of the Mo/GOx@HA

The strong oxidative power of •OH can convert TMB into a blue oxidation product (oxTMB), making TMB an effective substrate for confirming the peroxidase-like activity of Mo-zyme,as depicted in Fig. 3A. When H_2O_2 is introduced into the TMB solution, Mo-zyme catalyzes the oxidation of TMB to oxTMB, resulting in a dark blue solution and a prominent UV peak at 652 nm. In contrast, negligible color and absorbance changes are observed when H_2O_2 or Mo-zyme is used alone, confirming the peroxidase-like capability of Mo-zyme. TA serves as a fluorescent probe for •OH detection, validating the catalytic process further. Neither Mo-zyme nor H_2O_2 alone exhibits significant changes in fluorescence signals. However, a notable fluorescence signal at 435 nm (Fig. 3B) indicates the generation of •OH by Mo-zyme through the catalysis of H_2O_2, leading to the conversion of TA to highly fluorescent TAOH [39]. Previous studies have highlighted Mo-zyme's potential as an antibacterial agent due to its robust peroxidase-like activity [40,41].

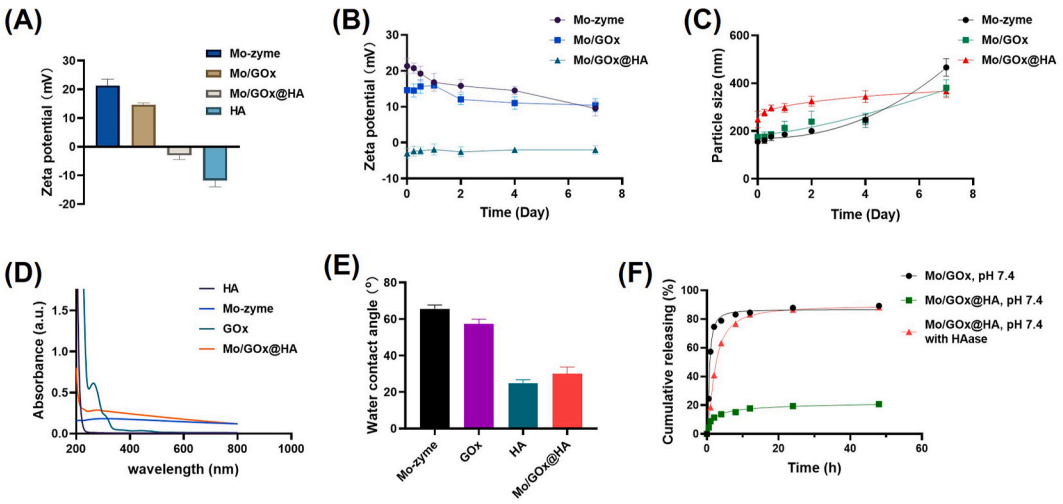

Fig. 2. (A) Zeta potential measurements for Mo-zyme, GOx, HA, and Mo/GOx@HA., (B) Zeta potential stability of Mo-zyme, Mo/GOx, and Mo/GOx@HA over 7 days in deionized water., (C) Particle size stability of Mo-zyme, Mo/GOx, and Mo/GOx@HA over 7 days in deionized water., (D) The UV spectrum of HA, Mo-zyme, GOx, and Mo/GOx@HA. (E) Water contact angle of HA, Mo-zyme, GOx, and Mo/GOx@HA, (F) Kinetic release profiles of GOx in PBS (pH 7.4) under various conditions.

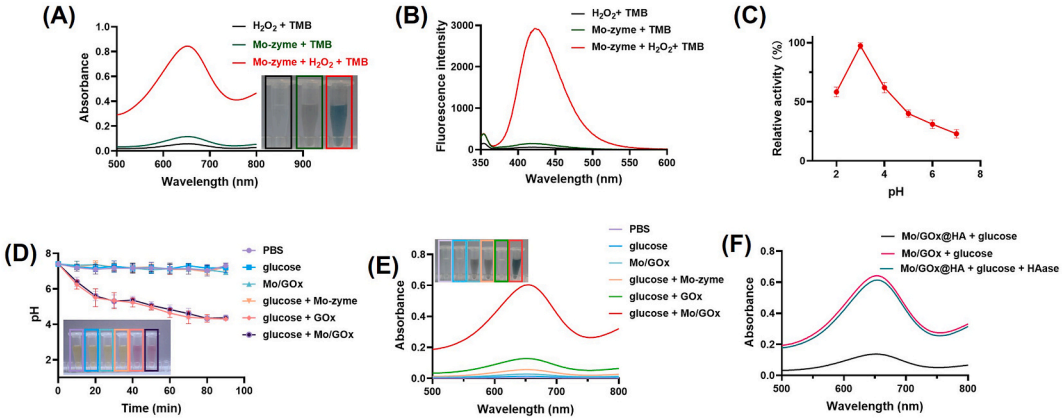

Fig. 3. (A) The UV spectrum of TMB with different treatment, (B) The fluorescence spectrum of TMB with different treatment, (C) Peroxidase-like activity of Mo-zyme at different pH values, (D) pH variation over time in different reaction systems, with an inset showing the corresponding digital photo in the presence of methyl red, (E) The UV–Vis spectrum and digital photo of different systems in the presence of TMB, (F) The fluorescence spectrum of TA with different treatment.

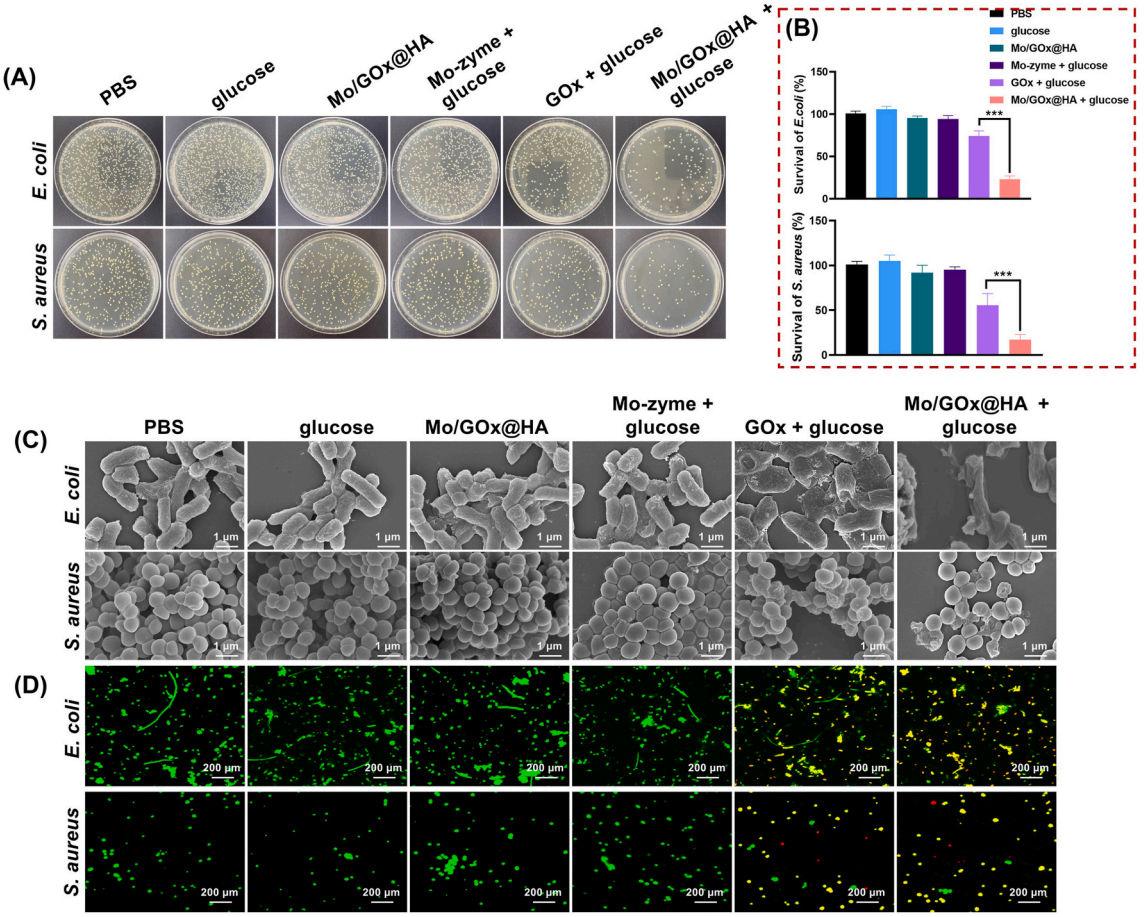

Fig. 4. (A) Digital photo of bacterial colonies and (B) survival rates of *S. aureus* and *E. coli* with different treatment, (C) SEM of *S. aureus* and *E. coli* with different treatment, (D) CLSM of *S. aureus* and *E. coli* with different treatment, and the green (SYTO 9) and red fluorescence (PI) represent respectively live and dead bacteria.

However, in vivo applications depend on pH sensitivity (Fig. 3C). Mo-zyme displays reduced catalytic activity under near-neutral conditions, which could limit its effectiveness in bacterial infection microenvironments. To enhance antibacterial efficacy, high concentrations of H_2O_2 are required to generate sufficient •OH. Alternatively, Mo-zyme can produce •OH through a cascade process involving glucose and GOx. This approach facilitates the development of potent bactericides without relying on exogenous H_2O_2, thereby mitigating potential side effects. To further explore the cascade catalytic properties of Mo/GOx, different systems are evaluated, and their pH changes are monitored (Fig. 3D, inset illustrates the solution color change recorded using methyl red). Coexistence of glucose and Mo/GOx significantly lowers the pH, similar to systems with glucose and pure GOx at equivalent concentrations. Upon addition of TMB, the glucose and Mo/GOx system turns blue with a distinct absorption peak at 652 nm (Fig. 3E), contrasting with minimal changes in color and absorbance in other systems. This outcome underscores the successful completion of the cascade catalytic process, initiated by glucose catalysis and subsequent •OH generation facilitated by Mo-zyme's single-atom catalytic activity.

To mitigate the early release of GOx from Mo-zyme and thereby reduce potential side effects on normal tissues and cells, HA is used to encapsulate GOx within Mo-zyme. Subsequently, the feasibility of an HAase-mediated cascade process is explored, as illustrated in Fig. 3F. When glucose is treated with Mo/GOx, a prominent absorbance peak at 652 nm indicated glucose catalysis by encapsulated GOx. In contrast, only a slight absorbance at the same wavelength is observed when glucose is treated with Mo/GOx@HA. Importantly, upon HAase participation, the absorbance of glucose at 652 nm after treatment with Mo/GOx@HA closely resembles that of glucose treated with Mo/GOx, providing strong evidence that the HAase-mediated cascade process is practical and feasible.

3.4. Evaluation of antibacterial ability in vitro

To evaluate the antibacterial efficacy of Mo/GOx@HA against classical Gram-positive (*S. aureus*) and Gram-negative (*E. coli*) strains, further investigations are conducted. Initially, logarithmic phase cultures of *S. aureus* and *E. coli* are treated with various agents: (1) PBS, (2) glucose, (3) Mo/GOx@HA, (4) glucose + Mo-zyme, (5) glucose + GOx, and (6) glucose + Mo/GOx@HA. The results of colony cultures and bacterial survival rates, as shown in Fig. 4A and B, reveal that the survival rates of bacteria in groups (2)−(4) are similar to group (1). However, only 55.7 % and 74.3 % of *S. aureus* and *E. coli*, respectively, survived in group (5), indicating limited antibacterial activity from H_2O_2 produced by glucose oxidation alone. Importantly, the survival rates of *S. aureus* and *E. coli* in group (6), treated with both glucose and Mo/GOx@HA, are significantly lower at 5.41 % and 8.32 %, respectively. This outcome underscores the effectiveness of the catalytic cascade reaction, where H_2O_2 produced by glucose oxidation is further catalyzed to generate more antibacterially active •OH.

Considering the potential impact on the morphology of *S. aureus* or *E. coli* due to changes in membrane permeability and integrity of deceased strains [42,43], the study utilizes scanning electron microscopy to analyze their morphology under various treatments, as shown in Fig. 4C. The morphology of strains treated with glucose, Mo/GOx@HA, or glucose + Mo-zyme closely resembles that of the PBS group. However, strains treated with glucose + GOx exhibit slight wrinkling, indicating a mild antibacterial effect exerted by generated H_2O_2. Significantly, strains treated with glucose + Mo/GOx@HA showed severe membrane damage, characterized by irregular voids on their surfaces. This suggests substantial oxidative damage inflicted by •OH produced during the catalytic cascade reaction.

To visualize the antibacterial performance of Mo/GOx@HA, live/dead bacterial staining is conducted on strains subjected to different treatments. Although the green and red dots represent live and dead bacteria, respectively, Fig. 4D provides a clearer merged image (yellow dots) for a more accurate description of dead bacteria. Most strains exhibit survival in the absence of GOx catalysis, as

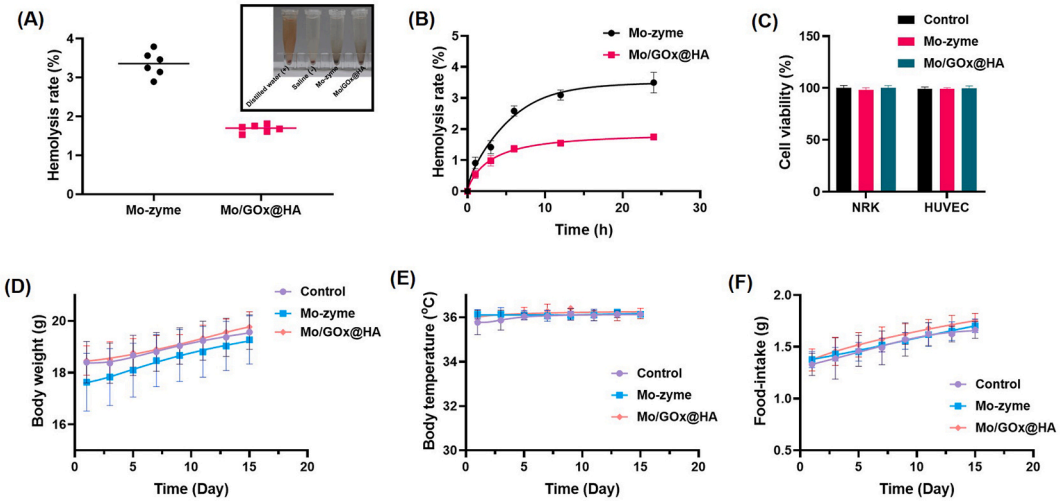

Fig. 5. (A) Hemolysis test of Mo-zyme and Mo/GOx@HA with the concentrations of 500 μg/mL, (B) Relative hemolysis ratio of Mo-zyme and Mo/GOx@HA in 24 h, (C) Cytotoxicity of Mo-zyme and Mo/GOx@HA to NRK and HUCEV cells, (D)–(F) Body weight, body temperature and food-intake of mice with diferent treatment in 15 days, respectively.

indicated by predominantly green fluorescence. In contrast, the presence of red fluorescence in the glucose + GOx group suggested enhanced antibacterial effects attributed to H_2O_2 generated from glucose oxidation. Importantly, the significant overlap of green and red dots in strains treated with Mo/GOx@HA indicates a marked enhancement in antibacterial efficacy due to the catalytic cascade reaction. This observation is consistent with the results obtained from colony counts, highlighting the potent antibacterial potential of Mo/GOx@HA.

3.5. Biosafety evaluation of Mo/GOx@HA

As a nanodrug developed for bacterial infection treatment, ensuring robust biosafety is crucial prior to clinical use. Therefore, a hemolysis assay is initially conducted, indicating that both Mo-zyme and Mo/GOx@HA (Fig. 5A) exhibit hemolysis rates consistently below 5 %. This excellent hemocompatibility is sustained within 24 h (Fig. 5B), confirming their suitability for biomedical applications [33]. Cytotoxicity assessments on HUVEC and NRK cells (Fig. 5C) demonstrate over 95 % cell viability even at concentrations up to 500 μg/mL compare to controls, indicating non-toxicity to normal cells. These results underscore the safety of the nanodrug. Observations of vital signs over 15 days post-treatment in mice (Fig. 5D–F) reveal no significant impact on growth, highlighting the reliable safety profile of Mo-zyme and Mo/GOx@HA for potential biomedical applications.

To further evaluate the biosafety of the nanodrug in mice, hematoxylin and eosin staining (H&E) of major organs collected seven days after intravenous administration of the nanomaterials was conducted, as shown in Fig. 6A. The results show no significant histopathological changes in the main organs across different treatment groups. Moreover, Mo-zyme and Mo/GOx@HA did not significantly affect serum biochemical markers in mice (Fig. 6B–E), including ALT, AST, ALP, and others, indicating no impairment of liver or kidney function. These findings support the potential medical applications of Mo-zyme and suggest Mo/GOx@HA could be further developed for the treatment of bacterial infections.

3.6. Antibacterial activity of Mo/GOx@HA in vivo

To evaluate the antibacterial properties of Mo/GOx@HA, a bacterial infection model was established on BALB/c mice using skin wounds. The mice were randomly divided into six groups, each receiving a different treatment. Although wounds in mice treated with PBS, glucose, Mo/GOx@HA, and glucose + Mozyme all showed varying degrees of healing (Fig. 7A), this could be attributed to natural self-healing. However, the wound tissue treated with glucose + GOx demonstrated significantly better recovery, suggesting that GOx can effectively catalyze glucose into antibacterial H_2O_2. Notably, in mice treated with glucose + Mo/GOx@HA, the wounds were clearly covered with regenerated skin, indicating that the cascade catalytic system exhibits excellent antibacterial activity at the site of

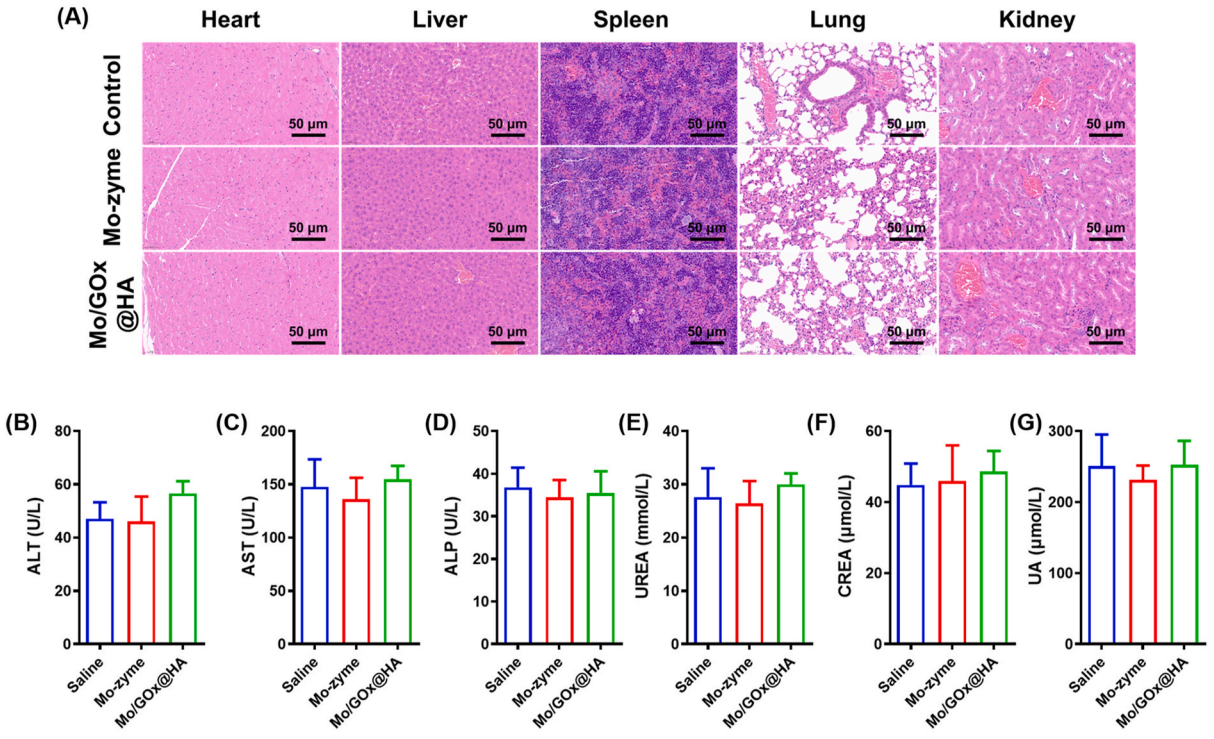

Fig. 6. (A) H&E staining of major mice organs after diferent treatment, (B)–(E) ALT, AST, ALP, UREA, CREA and UA indexes of mice with diferent treatment, respectively.

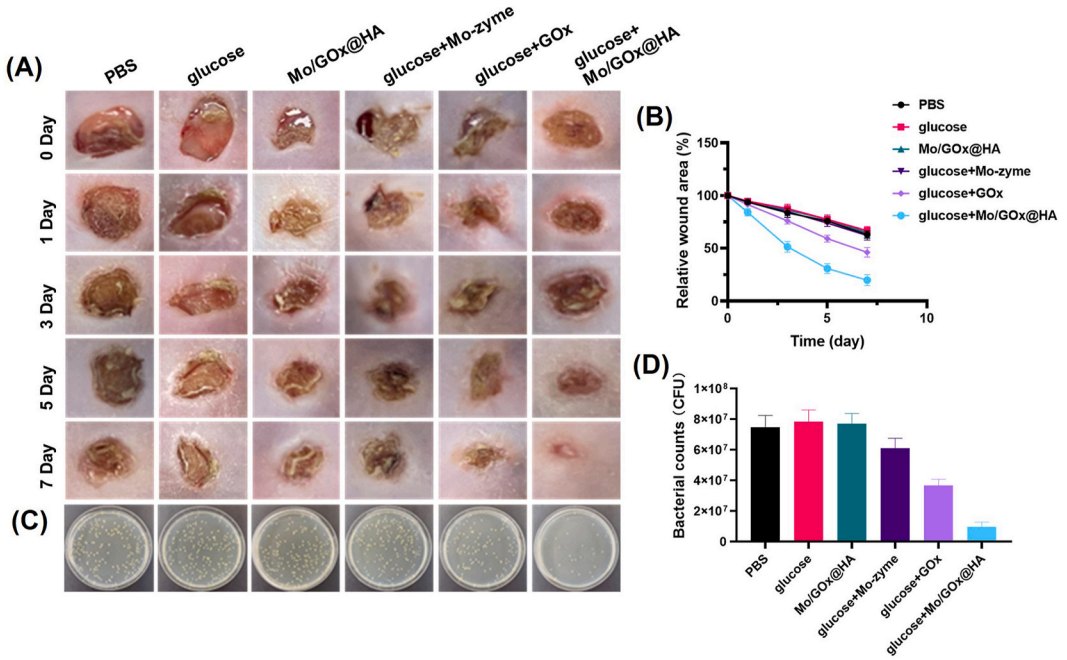

Fig. 7. (A) Digital photo of *S. aureus* infected wounds with different treatment in 7 days, (B) Relative wound area during different treatment, (C) Bacterial colonies of different wound tissue when treatment was ended, (D) Bacterial counts of different wound tissue when treatment was ended.

infected wounds. After 7 days of continuous treatment, wound area analysis using Image J reveals significant reduction and nearly complete healing (Fig. 7B), indicating Mo/GOx@HA effectively inhibits bacterial infection by enhancing •OH production through catalytic cascade reactions. For quantitative assessment of antimicrobial effects, colony counting is performed after homogenizing the wound tissue at the end of treatment (Fig. 7C and D). The results show a significant decrease in colony counts when wounds were treated with Mo/GOx@HA, with survival bacterial counts reduced to only 9.64 % compared to PBS-treated wounds. In contrast, treatment with glucose + GOx results a slight decrease in survival bacteria, with counts still high at 49.15 % compared to PBS treatment. These findings suggest that the antibacterial effect of •OH generated through cascade catalysis is more promising than that of H_2O_2 generated from glucose oxidation.

Different types of staining are performed on wound tissues to further evaluate infection healing and changes in inflammatory cytokines, as shown in Fig. 8A. Unlike treatments showing abundant inflammatory cells and incomplete epidermal structures, H&E staining of infected wounds treated with Mo/GOx@HA reveals a significant decrease in inflammatory cells and a relatively complete epidermal structure. Masson staining indicates maximal collagen fiber formation, suggesting thorough infection treatment by Mo/GOx@HA. Interleukin-6 (IL-6) levels, a typical inflammatory cytokine, demonstrate an improved inflammatory response in wounds treated with Mo/GOx@HA. These results underscore the enhanced antibacterial effect of Mo/GOx@HA through cascade catalysis for •OH generation, effectively inhibiting infection, down-regulating IL-6 expression, and promoting wound healing. To further assess changes in the immune microenvironment during wound healing, levels of proinflammatory cytokines (IL-6 and IL-1β) and anti-inflammatory cytokines (IL-10 and TGF-β) in wound tissue are measured using ELISA (Fig. 8B–E). Proinflammatory cytokines IL-6 and IL-1β decreased in Mo/GOx@HA-treated wounds in the presence of glucose when the mice treated with Mo/GOx@HA, while anti-inflammatory cytokines IL-10 and TGF-β were significantly elevated (Fig. 8F). These findings indicate that the cascade catalysis process effectively modulates the inflammatory microenvironment by enhancing anti-inflammatory cytokines, thereby improving wound infection immunomodulation.

4. Conclusions

In this study, a positively charged molybdenum-derived single-atom nanozyme (Mo-zyme) was synthesized by coordinating single-atom molybdenum with nitrogen atoms within a zeolitic imidazolate framework (ZIF-8). Glucose oxidase (GOx) was subsequently loaded onto Mo-zyme, and hyaluronic acid (HA) was encapsulated through electrostatic attraction, resulting in the formation of the Mo/GOx@HA complex. This complex demonstrates cascade catalytic properties, utilizing bacteria-secreted hyaluronidase to initiate a cascade reaction that continuously generates hydrogen peroxide (H_2O_2) at the site of wound infection. This catalytic process effectively treats bacterial infections. This research introduces a novel approach for developing cascade catalytic systems for antibacterial applications and underscores the potential of molybdenum-derived single-atom nanozymes in biomedical fields.

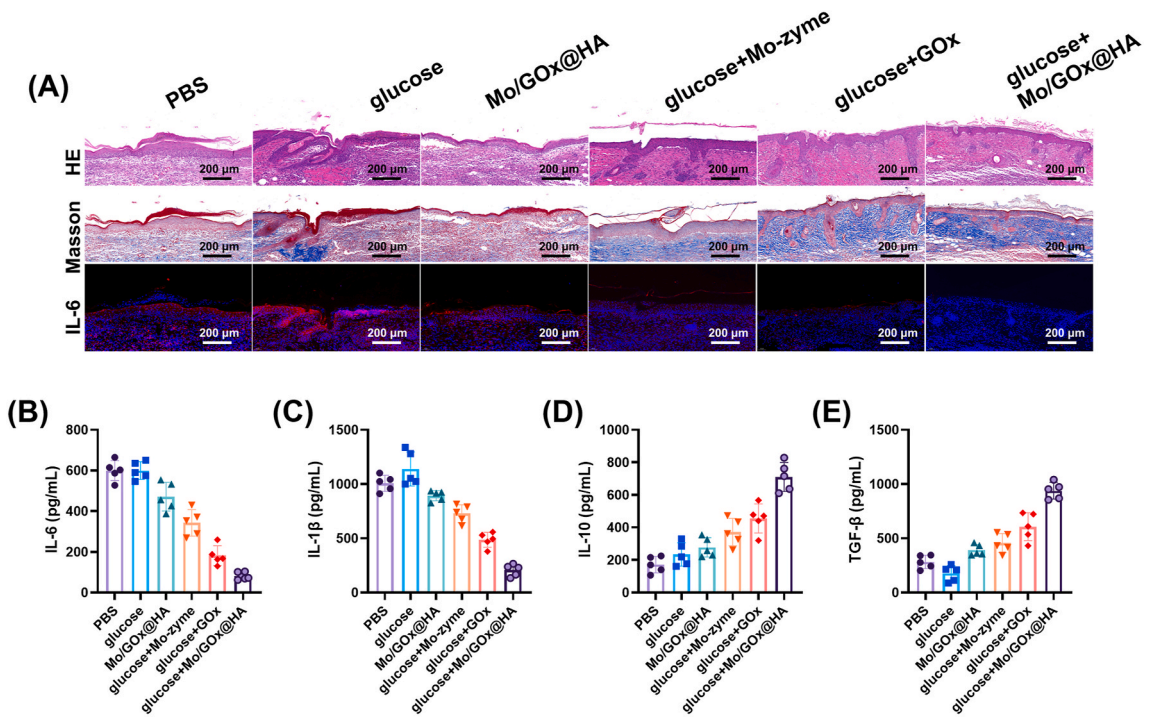

Fig. 8. (A) H&E staining, Masson staining and immunofluorescence staining of IL-6 of wounds when the treatment was ended, (B)–(E) IL-6, IL-1β, IL-10 and TGF-β levels in different wound tissue when the treatment was ended, respectively.

Ethics statement

All animal-related procedures were conducted in accordance with the guidelines of the China Council on Animal Care and the Ministry of Agriculture of the People's Republic of China. All Animal experiments reported in this study were reviewed and approved by the Institutional Animal Care and Use Committee of the Xi'an Jiaotong University (Permit No: IACUC-20230059).

Data availability

The raw/processed data required to reproduce these findings cannot be shared at this time due to technical or time limitations.

CRediT authorship contribution statement

Haoruo Jia: Writing – review & editing, Writing – original draft, Visualization, Validation, Supervision, Software, Resources, Methodology, Investigation, Formal analysis, Data curation, Conceptualization. **Ziyuan Zheng:** Writing – original draft, Visualization, Validation, Software, Methodology, Investigation, Formal analysis, Data curation. **Jining Qu:** Writing – original draft, Validation, Software, Methodology, Investigation, Formal analysis, Data curation. **Hongtao Yu:** Validation, Methodology, Investigation. **Zhoujun Zhu:** Writing – original draft, Methodology, Investigation, Formal analysis, Data curation. **Qingda Lu:** Validation, Methodology, Investigation, Formal analysis, Data curation. **Fei Su:** Validation, Methodology, Investigation, Formal analysis, Data curation. **Yating Yang:** Validation, Methodology, Investigation, Formal analysis, Data curation. **Tongtong Feng:** Visualization, Methodology, Investigation, Formal analysis, Data curation. **Qiang Jie:** Writing – review & editing, Writing – original draft, Visualization, Validation, Resources, Project administration, Funding acquisition, Formal analysis, Data curation, Conceptualization.

Declaration of competing interest

The authors declare that they have no known competing financial interests or personal relationships that could have appeared to influence the work reported in this paper.

Acknowledgements

This work was supported by the National Natural Science Foundation of China (Grant No. 81702164, 82272442), Clinincal Research Center for Pediactric Skeletal Deformity and Injury of Shaanxi Province (Grant No. 2024SF-LCZX-16), Platform construction

project of Shaanxi province health scientific research innovation ability promotion plan (Grant No. 2024 PT-12), Clinical Medical Research Center Projects-Innovation Capability Support Program of Shaanxi Province (Grant No. 2020LCZX-03), Innovation Capability Support Program of Shaanxi Province (Grant No. 2020TD-036).

Appendix A. Supplementary data

Supplementary data to this article can be found online at https://doi.org/10.1016/j.heliyon.2024.e38057.

References

[1] Y. Bian, K. Zhao, T. Hu, C. Tan, R. Liang, X. Weng, Nanoparticle/MgFe-LDH composite nanosheet as a multifunctional Platform for osteosarcoma eradication, antibacterial and bone reconstruction, Adv. Sci. (2024) 2403791, https://doi.org/10.1002/advs.202403791.
[2] D.R. Long, C. Bryson-Cahn, A. Waalkes, E.A. Holmes, K. Penewit, C. Tavolaro, C. Bellabarba, F. Zhang, J.D. Chan, F.C. Fang, J.B. Lynch, S.J. Salipante, Contribution of the patient microbiome to surgical site infection and antibiotic prophylaxis failure in spine surgery, Sci. Transl. Med. 742 (2024) eadk8222, https://doi.org/10.1126/scitranslmed.adk8222.
[3] R. Lu, Y. Zhang, J. Chen, Y. Zhang, C. Zhang, A multifunctional tissue-engineering hydrogel aimed to regulate bacterial ferroptosis-like death and overcoming infection toward bone remodeling, Adv. Sci. (2024) e2309820, https://doi.org/10.1002/advs.202309820.
[4] S. Helaine, B.P. Conlon, K.M. Davis, D.G. Russell, Host stress drives tolerance and persistence: the bane of anti-microbial therapeutics, Cell Host Microbe 6 (2024) 852–862, https://doi.org/10.1016/j.chom.2024.04.019.
[5] A. Abbas, A. Barkhouse, D. Hackenberger, G.D. Wright, Antibiotic resistance: a key microbial survival mechanism that threatens public health, Cell Host Microbe 6 (2024) 837–851, https://doi.org/10.1016/j.chom.2024.05.015.
[6] S. Liu, S.Y. Quek, K. Huang, An ecofriendly nature-inspired microcarrier for enhancing delivery, stability, and biocidal efficacy of phage-based biopesticides, Small (2024) e2403465, https://doi.org/10.1002/smll.202403465.
[7] X. Zhao, X. Zhong, S. Yang, J. Deng, K. Deng, Z. Huang, Y. Li, Z. Yin, Y. Liu, J.H. Viel, H. Wan, Guiding antibiotics towards their target using bacteriophage proteins, Nat. Commun. 1 (2024) 5287, https://doi.org/10.1038/s41467-024-49603-4.
[8] C.K.O. Dzuvor, H.H. Shen, V.S. Haritos, L. He, Coassembled multicomponent Protein nanoparticles elicit enhanced antibacterial activity, ACS Nano 5 (2024) 4478–4494, https://doi.org/10.1021/acsnano.3c11179.
[9] Z. Xing, J. Guo, Z. Wu, C. He, L. Wang, M. Bai, X. Liu, B. Zhu, Q. Guan, C. Cheng, Nanomaterials-enabled physicochemical antibacterial therapeutics: toward the antibiotic-free disinfections, Small 50 (2023) e2303594, https://doi.org/10.1002/smll.202303594.
[10] Z. Wang, X. Liu, Y. Duan, Y. Huang, Infection microenvironment-related antibacterial nanotherapeutic strategies, Biomaterials (2022) 121249, https://doi.org/10.1016/j.biomaterials.2021.121249.
[11] L. Yao, Q. Liu, Z. Lei, T. Sun, Development and challenges of antimicrobial peptide delivery strategies in bacterial therapy: a review, Int. J. Biol. Macromol. 253 (2023) 126819, https://doi.org/10.1016/j.ijbiomac.2023.126819.
[12] J. Zeng, Y. Hong, N. Zhao, Q. Liu, W. Zhu, L. Xiao, W. Wang, M. Chen, S. Hong, L. Wu, Y. Xue, D. Wang, J. Niu, K. Drlica, X. Zhao, A broadly applicable, stress-mediated bacterial death pathway regulated by the phosphotransferase system (PTS) and the cAMP-Crp cascade, Proc. Natl. Acad. Sci. U.S.A. 119 (2022) e2118566119, https://doi.org/10.1073/pnas.2118566119.
[13] Y. Wang, Y. Xu, X. Guo, L. Wang, J. Zeng, H. Qiu, Y. Tan, D. Chen, H. Zhao, Y. Gu, Enhanced antimicrobial activity through the combination of antimicrobial photodynamic therapy and low-frequency ultrasonic irradiation, Adv. Drug Deliv. Rev. 183 (2022) 114168, https://doi.org/10.1016/j.addr.2022.114168.
[14] Y. Yang, Z. Li, X. Fan, C. Jiang, J. Wang, Y. Rastegar-Kashkooli, T.J. Wang, M. Wang, N. Cheng, X. Yuan, X. Chen, B. Jiang, J. Wang, Nanozymes: potential therapies for reactive oxygen species overproduction and inflammation in ischemic stroke and traumatic brain Injury, ACS Nano 18 (2024) 16450–16467, https://doi.org/10.1021/acsnano.4c03425.
[15] W. Wang, T. Wang, S. Chen, Y. Lv, L. Salmon, B. Espuche, S. Moya, O. Morozova, Y. Yun, D. Di Silvio, N. Daro, M. Berlande, P. Hapiot, J.L. Pozzo, H. Yu, J. R. Hamon, D. Astruc, Cu(I)-Glutathione assembly supported on ZIF-8 as robust and efficient catalyst for mild CO_2 conversions, Angew. Chem. Int. Ed. (2024) e202407430, https://doi.org/10.1002/anie.202407430.
[16] R.F. Zhang, B. Jiang, K.L. Fan, L.Z. Gao, X.Y. Yan, Designing nanozymes for in vivo applications, Nat. Rev. Bioeng (2024), https://doi.org/10.1038/s44222-024-00205-1.
[17] Z. Yue, J. Li, M. Tang, T. Sun, C. Chen, Z. Wu, Nanozyme-based clusterphene for enhanced electrically catalytic cancer therapy, Adv. Healthcare Mater. 9 (2024) e2303222, https://doi.org/10.1002/adhm.202303222.
[18] S.F. Zhang, X.D. Zhang, Recent advances in the bioactive structure and application of single-atom nanozymes, Nano Biomed. Eng. 1 (2024) 1–27, https://doi.org/10.26599/NBE.2023.9290047.
[19] B.L. Xu, H. Wang, W.W. Wang, L.Z. Gao, S.S. Li, X.T. Pan, H. Y Wang, H.L. Yang, X.Q. Meng, Q.W. Wu, L.R. Zheng, S.M. Chen, X.H. Shi, K.L. Fan, X.Y. Yan, H. Y. Liu, A single-atom nanozyme for wound disinfection applications, Angew. Chem. Int. Ed. 15 (2019) 4911–4916, https://doi.org/10.1002/anie.201813994.
[20] Z. Fu, K. Fan, X. He, Q. Wang, J. Yuan, K.S. Lim, J.N. Tang, F. Xie, X. Cui, Single-atom-based nanoenzyme in tissue repair, ACS Nano 21 (2024) 12639–12671, https://doi.org/10.1021/acsnano.4c00308.
[21] X. Lan, M. Chen, X. He, S. Gao, X. Zhao, Single atom nanozymes for bacterial infection therapy, Biomater. Sci. 12 (2023) 108–115, https://doi.org/10.1039/d3bm01838e.
[22] Q. Wang, J. Jiang, L. Gao, Catalytic antimicrobial therapy using nanozymes, Wiley Interdiscip. Rev. Nanomed. Nanobiotechnol. 14 (2022) e1769, https://doi.org/10.1002/wnan.1769.
[23] X. Mou, Q. Wu, Z. Zhang, Y. Liu, J. Zhang, C. Zhang, X. Chen, K. Fan, H. Liu, Nanozymes for regenerative medicine, Small Methods 6 (2022) e2200997, https://doi.org/10.1002/smtd.202200997.
[24] B. Qiao, A. Wang, X. Yang, F. Lawrence, Z. Jiang, Y. Cui, J. Liu, J. Li, T. Zhang, Single-atom catalysis of CO oxidation using Pt_1/FeOx, Nat. Chem. 3 (2011) 634–641, https://doi.org/10.1038/nchem.1095.
[25] X. Liao, J. Wang, B. Guo, M. Bai, Y. Zhang, G. Yu, P. Wang, J. Wei, J. Wang, X. Yan, K. Fan, Y. Wang, Enhancing nanobody immunoassays through ferritin fusion: construction of a salmonella-specific fenobody for improved avidity and sensitivity, J. Agric. Food Chem. 72 (2024) 14967–14974, https://doi.org/10.1021/acs.jafc.4c03606.
[26] H. Liu, B. Yu, P. Yang, Y. Yang, Z. Deng, X. Zhang, K. Wang, H. Wang, Axial O atom-modulated Fe(III)-N_4 sites for enhanced cascade catalytic $1O_2$-induced tumor therapy, Adv. Sci. (2024) e2307254, https://doi.org/10.1002/advs.202307254.
[27] W. Li, H. Huang, S. Yao, Y. Zhao, M. Liu, X. Liu, H. Guo, Engineering of a double targeting nanoplatform to elevate ROS generation and DSF anticancer activity, J. Mater. Chem. B (2024), https://doi.org/10.1039/d4tb00455h.
[28] X. Zhang, Q. Zong, T. Lin, I. Ullah, M. Jiang, S. Chen, W. Tang, Y. Guo, Y. Yuan, J. Du, Self-assembled metal-phenolic network nanoparticles for delivery of a cisplatin prodrug for synergistic chemo-immunotherapy, Biomater. Sci. (2024), https://doi.org/10.1039/d4bm00650j.
[29] Q. Wang, C. Zhang, Y. Zhao, S. Zhou, J. Qin, W. Zhang, Y. Hu, X. Chen, K. Yang, Polyprodrug nanomedicine for chemiexcitation-triggered self-augmented cancer chemotherapy and gas therapy, Biomaterials 309 (2024) 122606, https://doi.org/10.1016/j.biomaterials.2024.122606.

[30] W. Xu, Y. Zhang, X. Xu, J. Chen, Construction of Mo-based p-n heterojunction with enhanced oxidase-mimic activity for AOPs and antibiofouling, Inorg. Chem. 62 (2023) 14773–14781, https://doi.org/10.1021/acs.inorgchem.3c02249.
[31] H. Song, Z. Cheng, R. Qin, Z. Chen, T. Wang, Y. Wang, H. Jiang, Y. Du, F. Wu, Iron/molybdenum sulfide nanozyme cocatalytic fenton reaction for photothermal/chemodynamic efficient wound healing, Langmuir (2024), https://doi.org/10.1021/acs.langmuir.4c00922.
[32] J. Zhao, Q. Sun, D. Mo, J. Feng, Y. Wang, T. Li, Y. Zhang, H. Wei, A self-cascade oxygen-generating nanomedicine for multimodal tumor therapy, Small (2024) e2403523, https://doi.org/10.1002/smll.202403523.
[33] J. Wang, Z. Zhang, Z. Yu, Y. Qiao, C. Wang, T. Yang, H. Wu, Polyglycerol-Decorated hollow mesoporous ruthenium nanoparticles for long circulation and antitumor effect, ACS Appl. Nano Mater. 10 (2023) 8695–8704, https://doi.org/10.1021/acsanm.3c01052.
[34] Y. Chen, P. Wang, H. Hao, J. Hong, H. Li, S. Ji, A. Li, R. Gao, J. Dong, X. Han, M. Liang, D. Wang, Y. Li, Thermal atomization of platinum nanoparticles into single atoms: an effective strategy for engineering high-performance nanozymes, J. Am. Chem. Soc. 44 (2021) 18643–18651, https://doi.org/10.1021/jacs.1c08581.
[35] M. Yang, W. Xu, Z. Chen, M. Chen, X. Zhang, H. He, Y. Wu, X. Chen, T. Zhang, M. Yan, Engineering hibiscus-like riboflavin/ZIF-8 microsphere composites to enhance transepithelial corneal cross-linking, Adv. Mater. 34 (2022) e2109865, https://doi.org/10.1002/adma.202109865.
[36] Y. Pan, Y. Chen, K. Wu, S. Liu, X. Cao, W.C. Cheong, T. Meng, J. Luo, L. Zheng, C. Liu, D. Wang, Q. Peng, J. Li, C. Chen, Regulating the coordination structure of single-atom Fe-NxCy catalytic sites for benzene oxidation, Nat. Commun. 10 (2019) 4290, https://doi.org/10.1038/s41467-019-12362-8.
[37] Y. Wang, G.R. Jia, X.Q. Cui, X. Zhao, Q.H. Zhang, L. Gu, L.R. Zheng, L.H. Li, Q. Wu, D.J. Singh, D. Matsumura, T. Tsuji, Y.T. Cui, J.X. Zhao, W.T. Zheng, Coordination number regulation of molybdenum single-atom nanozyme peroxidase-like specificity, Chem 7 (2021) 1–14, https://doi.org/10.1016/j.chempr.2020.10.023.
[38] J. Wang, Z. Guo, J. Xiong, D. Wu, S. Li, Y. Tao, Y. Qin, Y. Kong, Facile synthesis of chitosan-grafted beta-cyclodextrin for stimuli-responsive drug delivery, Int. J. Biol. Macromol. 125 (2019) 941–947, https://doi.org/10.1016/j.ijbiomac.2018.12.150. Biomaterials.
[39] Z. Liu, F. Wang, J. Ren, X. Qu, A Series of MOF/Ce-based Nanozymes with Dual Enzyme-like Activity Disrupting Biofilms and Hindering Recolonization of Bacteria, vol. 208, 2019, pp. 21–31, https://doi.org/10.1016/j.biomaterials.2019.04.007.
[40] Y. Li, R. Fu, Z. Duan, C. Zhu, D. Fan, Construction of multifunctional hydrogel based on the tannic acid-metal coating decorated MoS_2 dual nanozyme for bacteria-infected wound healing, Bioact. Mater. 9 (2022) 461–474, https://doi.org/10.1016/j.bioactmat.2021.07.023.
[41] T. Wang, X. Zhang, L. Mei, D. Ma, Y. Liao, Y. Zu, P. Xu, W. Yin, Z. Gu, A two-step gas/liquid strategy for the production of N-doped defect-rich transition metal dichalcogenide nanosheets and their antibacterial applications, Nanoscale 12 (2020) 8415–8424, https://doi.org/10.1039/d0nr00192a.
[42] Y. Guo, S. Ding, C. Shang, C. Zhang, M. Li, Q. Zhang, L. Gu, B.C. Heng, S. Zhang, F. Mei, Y. Huang, X. Zhang, M. Xu, J. Jiang, S. Guo, X. Deng, L. Chen, Multifunctional PtCuTe nanosheets with strong ROS scavenging and ROS-independent antibacterial properties promote diabetic wound healing, Adv. Mater. 36 (2024) e2306292, https://doi.org/10.1002/adma.202306292.
[43] X. Wu, M. Yang, J.S. Kim, R. Wang, G. Kim, J. Ha, H. Kim, Y. Cho, K.T. Nam, J. Yoon, Reactivity differences enable ROS for selective ablation of bacteria, Angew. Chem. Int. Ed. 61 (2022) e202200808, https://doi.org/10.1002/anie.202200808.